Experimental investigation of an active slat for airfoil load alleviation

P Singh,[1, a)] L Neuhaus,[1] O Huxdorf,[2] J Riemenschneider,[2] J Wild,[3] J Peinke,[1] and M Hölling[1]

[1)] *ForWind - Institute of Physics, University of Oldenburg, 26129 Oldenburg, Germany*

[2)] *DLR - Institute of Composite Structures and Adaptive Systems, 38108 Braunschweig, Germany*

[3)] *DLR - Institute of Aerodynamics and Flow Technology, 38108 Braunschweig, Germany*

(Dated: July 1, 2021)

This article discusses the utilisation of an active slat concept to reduce turbulence induced fluctuating loads on an airfoil. The performance of the active slat is tested in the wind tunnel under different complex inflows created by an active grid resulting into variations in the angle of attack. Different open loop control strategies are developed to mitigate the load fluctuations on the airfoil. The aerodynamics around the airfoil is changed by actively moving the trailing edge of the slat. It is observed that the active slat concept is able to alleviate load fluctuations on the airfoil for inflow angle fluctuations of different scales.

KEYWORDS

leading edge slat, active slat, active load control, turbulence, blade unsteady load, active grid

I. INTRODUCTION

Wind turbines experience various kinds of loads in their working lifetime. Their operation in the atmospheric boundary layer exposes them to turbulent wind fields. Turbulent structures of various scales and wind gusts causing inflow velocity fluctuations interact with the wind turbine blades[1,2]. As the inflow velocity is one of the main components for determining the angle of attack perceived by the sectional airfoils on a wind turbine blade, its fluctuation results in the unsteadiness in angle of attack as well. This induces unsteady loads on the wind turbine blade which can cause fatigue damage[3–5]. In a recent study by Rezaeiha et al.[6] it was found that more than 65 % of flapwise fatigue loads are due to turbulence. This is undesirable because of its deteriorating effect on the blade life and efficiency, ultimately leading to blade structural failure[7]. This is why reduction of these loads is important for the development of efficient modern wind turbines and for the reduction of the cost of wind energy.

Commonly, wind turbines rely on pitch control methods such as cyclic pitch control and individual pitch control (IPC) for attenuating certain loads[8,9]. The massive inertia of the entire blade inhibits the reaction of common blade pitch control to the high frequency turbulence induced load fluctuations. Also, as the turbulent wind field does not interact with all regions of the blade in the same way, devices which can influence local aerodynamics are the requirement of modern wind turbine rotors.

Recent years have seen the development of smart rotor concept through many passive and active flow control techniques which concentrate on implementation of sectional devices influencing the aerodynamics in specific regions of the blade[10–12]. Some of these include vortex generators, trailing edge flaps, adaptive camber airfoils, microtabs, synthetic jets among others[13]. Each of these devices in some way or the other change the local aerodynamics around a region of the blade to influence the loads. The trailing edge flap has become a widely researched control device in recent years[14–16]. Its popularity is based on the fact that it causes a shift of the lift curve in the linear region, thus providing good control opportunities. This makes the trailing edge flap suitable for application in the outboard region of the blade. The inboard region of a wind turbine blade uses thick airfoils which cannot be optimally twisted because of the structural limitations of the blade, thus causing them to experience early separation[17]. The separation can result into fluctuating loads on not just the concerned thick airfoil but the arising separation bubbles may also travel outboard and disrupt the aerodynamic performance of airfoils which have attached flow. The trailing edge flap is not effective in delaying the stall angle of the airfoil and thus is not suitable for use in this region of the blade. For inboard region application, the vortex generators are popular passive flow control devices which help in keeping the flow attached to the airfoil by delaying stall[18,19]. The last decade has also seen some work on leading edge slat concepts for power performance enhancement of wind turbine[20–22]. As compared to vortex generators leading edge slats have a much wider angle of attack range as well provide higher maximum lift values[23,24]. Fluctuations in the inflow velocity of a wind field significantly contribute to variations in the angle of attack for the airfoils in the inboard region of the blade. This is due to the smaller magnitude of rotational velocity caused by the proximity to the axis of rotation of the wind turbine. The issue with the vortex generators and fixed leading edge slats is that they are fixed and cannot be controlled according to the turbulence induced inflow fluctuations. In order to reduce fatigue loads and to extract more energy from the

[a)] piyush.singh@uni-oldenburg.de

root region, a flow control device is required which can provide the ability to actively control the aerodynamics of the airfoil as well as help in avoiding flow separation.

An actively deformable leading edge slat system for airfoil load mitigation was recently investigated in a wind tunnel by Neuhaus et al.[25]. The work focused on the characterisation and estimation of the concept's initial capabilities. It was reported that the leading-edge active slat significantly delays the stall to higher angles of attack. For a sinusoidal inflow, the active slat was able to reduce 20 % of the lift force fluctuations. It was also reported that there is a dependency of the lift coefficient on the gap size between the slat and the main body of the airfoil. As it was a preliminary investigation, this property was not utilised for designing the control strategy.

The present study takes the work of Neuhaus et al.[25] further by comprehensively gauging the performance of the active slat by testing it under complex inflow conditions. An active grid is used to create span-wise correlated inflow angle fluctuations with user-defined properties like different intermittency levels[26–28]. The active slat provides the ability to change the aerodynamic forces acting on the airfoil. Different open loop control strategies are designed and implemented which leverage this property of the active slat, to reduce the fluctuating aerodynamic forces under the influence of turbulent inflow conditions. The loads on the airfoil in the controlled slat cases are compared to the case where the slat is static.

The article begins with the presentation of the experimental setup in section II. This section in detail discusses the wind tunnel, active grid, measurement sensors and most importantly the airfoil with an integrated active slat. The characteristics of the different turbulent inflow cases is presented in section III. Section IV presents the method for generating the open loop control slat trajectory which is used to control the motion of the active slat. This is followed by the presentation and discussion of results in section V. Lastly section VI concludes the article.

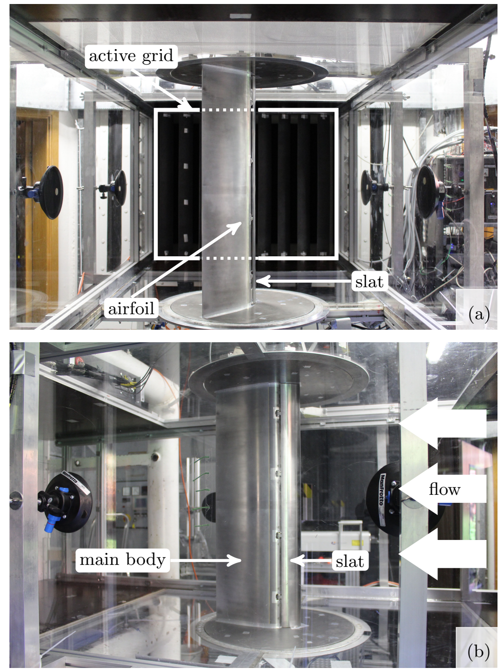

Figure 1: Active grid and airfoil with integrated active slat installed in the wind tunnel (a) and side view of the airfoil (b).

II. EXPERIMENTAL SETUP

The measurements presented in this work are performed in the Göttingen type wind tunnel at the University of Oldenburg. The wind tunnel has a test cross section of $1\,\mathrm{m} \times 0.8\,\mathrm{m}$ (width and height), while it is $2.6\,\mathrm{m}$ in length. Wind speeds up to $50\,\mathrm{m\,s^{-1}}$ can be generated in the wind tunnel. Turbulence intensity in laminar conditions have been reported to be around 0.3% by previous studies in the wind tunnel[29].

The inflow angle fluctuations are generated by using a special design of an active grid[30]. The active grid is mounted directly at the nozzle outlet of the wind tunnel and consists of 9 vertically mounted shafts which can be controlled independently. The rectangular profile and parallel orientation of these shafts with respect to the airfoil ensure that the entire span of the airfoil interacts with the same inflow at a given point in time (figure 1(a)). The inflow angle fluctuations generated by the active grid are measured prior to installation of the airfoil, in an empty wind tunnel. A X-type hot-wire is placed at the leading edge position of the airfoil located approximately 1 m downstream of the active grid. The sampling frequency of the hot wire measurement is 10 kHz.

The airfoil used in this measurement campaign has an integrated active slat (figure 1(b)). The airfoil's non deformed shape is based on the DU91-W2-250 airfoil. The design and optimisation of the integrated slat has been done by Manso et al.[31]. The airfoil has a thickness to chord ratio of 25 % with the chord being $c = 300\,\mathrm{mm}$. Reynolds number of up to $Re_c = 1 \times 10^6$ can be achieved with this experimental set-up. The airfoil was tripped in order trigger laminar turbulent transition and to prevent any separation arising from laminar separation bubble burst. The structural design of the slat was done by Huxdorf et al.[32]. The leading edge position of the slat remains fixed while the trailing edge of the slat can be moved by deforming the slat's compliant middle section on the pressure side using a stepper motor. For further details on the active slat structural design the reader is referred to the work of Huxdorf et al.[32]. The movement of the trailing edge of the slat changes the gap size g_s between the slat and the main body of the airfoil (figure 2). The gap size can be varied between $g_s/c = 1.06\%$ to $g_s/c = 2.83\%$ (3.18-8.49 mm). The non deformed slat position, which closely represents the clean profile is termed as the aerodynamic reference slat position. The corresponding gap size is the aerodynamic reference gap size and is defined as $g_{s,ref}/c = 2.05\%$.

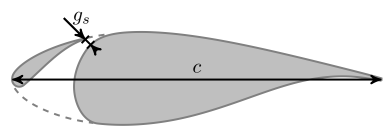

Figure 2: Investigated airfoil with controllable gap size g_s between slat and main body of the airfoil.

The wind tunnel's top and bottom walls have turn tables which are connected to a load cell for force and torque measurements. These measurements are done at a sampling frequency of 1 kHz. The airfoil is connected to the turntable on either side of its span. The axis of rotation of the turntable setup is at the quarter chord position of the airfoil. The airfoil is pitched about this axis using a stepper motor. The pitch angle of the airfoil is monitored using a directional sensor attached to the lower turntable. The humidity and temperature of the air is measured with a humidity-temperature sensor while the reference wind speed is measured from the dynamic pressure acquired using a differential pressure transducer.

III. COMPLEX INFLOW CHARACTERIZATION

The fluctuations of the inflow velocity as seen by a wind turbine directly translates into fluctuations in the angle of attack of the sectional airfoil. It is safe to say that any distinctive features in $u(t)$ would also migrate to $\alpha(t)$. Thus in this article the turbulent inflow is characterized in terms of the angle of attack variation with time.

A wind turbine normally comes across wind fields which are intermittent in nature. This means that the probability of occurrence of certain extreme events are higher than predicted by a Gaussian distribution[1]. An intermittent behaviour of the wind field contributes in increasing the damage equivalent load on the wind turbine blade[33,34]. A load mitigating device like the active slat should be able to operate and perform in wind conditions of varying levels of intermittency. Thus, to comprehensively gauge the performance of the active slat, it is subjected to various wind conditions. In order to estimate the operating range of the angle of attack in a real world scenario, the DU25-A17 airfoil located at 45 % of the rotor for the NREL 5 MW reference wind turbine is taken into consideration[35]. For the realistic estimation of the angle of attack, a section of the data measured at FINO1 site in North sea was taken into account. Considering an induction factor of 0.2 and twist angle of around 8° the inflow data is transformed into the airfoil coordinate system. The resultant angle of attack as seen by the airfoil has mean value of approximately $\overline{\alpha_r} = 10°$ and standard deviation of $\sigma_{\alpha_r} = 2°$. Taking into account the estimated operating range in a real world scenario, the active grid is used to create three distinct inflows, namely `Inflow1`, `Inflow2` and `Inflow3`. The inflow angle fluctuation time series for the three inflows is presented in figure 3. Each of the time series is 45 s long. The mean angle of attack $\overline{\alpha}$ for the inflows `Inflow1`, `Inflow2` and `Inflow3` are $-0.08°$, $-0.39°$ and $0.015°$, while the standard deviation σ_α for these are 1.29°, 1.77° and 1.16° respectively. For simulating the real world scenario, an airfoil pitch angle of 10° is later added to the inflow angle time series. Mean velocity of the wind field for all the three cases is around $30\,\mathrm{m\,s^{-1}}$, which corresponds to $Re_c = 6 \times 10^5$ for the airfoil.

When considering unsteady inflow fluctuations, one point statistics such as the standard deviation or mean do not fully characterize the inflow. While defining the inflow cases, it is imperative to understand the dynamics of the inflow-airfoil interaction. The unsteadiness associated with inflow and airfoil interaction is normally quantified by the reduced frequency

$$\kappa = \frac{2\pi . f . \frac{c}{2}}{\bar{u}} \tag{1}$$

It is defined by the frequency of inflow oscillation f, airfoil chord c and the mean velocity of the inflow $\bar{u}$. A purely sinusoidal inflow corresponds to one reduced frequency. A complex inflow can be seen as the combination of different periodic components and thus consists of a broad spectrum of reduced frequencies. In order for the generated inflows to distinctly interact with the airfoil, they should have different distribution of the reduced frequencies. A detailed insight in the distribution can be gained by plotting the power spectral density as a function of reduced frequency. The power spectra of the three inflows are plotted in figure 4. Also presented is the 1P reduced frequency range for a typical modern wind turbine. Pereira et al.[36] reported that the 1P reduced frequency for a wind turbine can be calculated from the local blade chord to radius ratio. For this definition, the authors assumed that the mean velocity of inflow as seen by the local airfoil is equal to the angular velocity of the airfoil. Although this is an approximation, it can provide a good estimate of the range of reduced frequencies associated with the interaction of natural flows with wind turbines. Using the parameters of the DTU 10 MW reference turbine[37], the 1P reduced frequency range for a typical modern wind turbine is calculated to be in

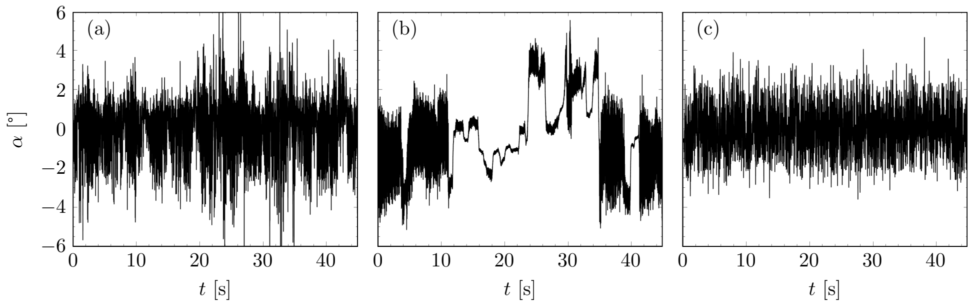

Figure 3: Turbulent inflow time series for different cases, `Inflow1` (a), `Inflow2` (b), `Inflow3` (c)

between $\kappa = 0.004$ to $\kappa = 0.17$. Leishman[38] associated reduced frequencies $\kappa < 0.05$ to quasi steady, $\kappa > 0.05$ to unsteady and $\kappa > 0.2$ to highly unsteady effects. Thus modern wind turbines experience a broad range of unsteady loads.

In figure 4 a clear difference in the energy distribution over different scales are observed for the power spectra of the three inflows. The power spectrum for `Inflow1` has high values for low reduced frequencies. As the reduced frequency increases the power spectrum drops a little and stabilizes in the range of $\kappa = 0.05$ to $\kappa = 0.5$. This indicates that `Inflow1` has significant quasi steady effects along with highly unsteady components. For `Inflow2` on the other hand, the energy content for the low reduced frequencies is very high and there is a high gradient in the power spectrum resulting in significantly lower energy content for larger reduced frequencies. This indicates at the dominant presence of quasi steady effects in the inflow. The power spectrum for `Inflow3` is nearly flat till $\kappa = 1$. This shows that `Inflow3` has white noise characteristics with no dominant structure present. Its interaction with the airfoil will be largely unsteady.

The power spectral density provides a good insight on the energy distribution over different scales but does not give any information on the time evolution of the inflow. More information regarding this can be obtained by analysing the statistics of two temporally separated points. This helps in determining the evolution in time as well as provides an estimation of the intermittent behaviour of the flow. The temporal velocity increments of intermittent flows are known to display non-Gaussian statistics, in particular for the probability density functions[1]. Deriving from the discussion above, the inflow angle fluctuation increments,

$$\alpha_\tau(t) = \alpha(t+\tau) - \alpha(t) \tag{2}$$

would also showcase a similar behaviour. Here τ is the time scale of the increment. The shape parameter,

$$\lambda^2(\tau) = \frac{1}{4}\ln\left(\frac{\left\langle(\alpha_\tau - \overline{\alpha_\tau})^4\right\rangle}{3\sigma_{\alpha_\tau}^4}\right) \tag{3}$$

is commonly used to characterise the intermittency in a flow field. Here $\overline{\alpha_\tau}$ and σ_{α_τ} are the mean and standard deviation of α_τ. It mainly determines the shape of the increment PDFs. It is 0 for the Gaussian distribution and has positive values for intermittent distribution. Higher values of $\lambda^2(\tau)$ indicate higher level of intermittency at the time scale τ. For more details on the shape factor and intermittency the reader is referred to the work of Castaing et al.[39] and Morales et al.[40] amongst others.

The different complex inflows which are generated, aerodynamically interact with the airfoil. Thus, when talking about intermittent characteristics of the flow the relevant length and time scales should be considered. As we are interested in the dynamic response of the airfoil, its chord length is used as the characteristic length. The relevant time scales for the present system can be computed from the chord length and the mean wind speed using the Taylor's hypothesis of frozen turbulence. For a Reynolds number of 6×10^5, the time scale corresponding to the airfoil chord is about 0.01 s. It is expected that the characteristics of the inflow with time scales higher than 0.01 s would significantly influence the airfoil as well.

The PDFs of the increments inflow angle fluctuations for scale τ of 0.002 s, 0.010 s, 0.041 s, 0.167 s and 0.673 s are plotted in figure 5 (a), (c) and (e). The time scales are logarithmically equidistant. The X axis of the increment PDFs have been normalised by the standard deviation of the respective inflow angle fluctuation increments. Gaussian PDF fits for each increment PDF have been added to the plots for a comparison to the Gaussian distribution. Also presented in these figure 5 (b), (d) and (f) are the shape parameter variations for the three inflows with respect to the time scale τ.

When examining the behaviour of `Inflow1` in figure 5 (a), it is observed that all the PDFs corresponding to dif-

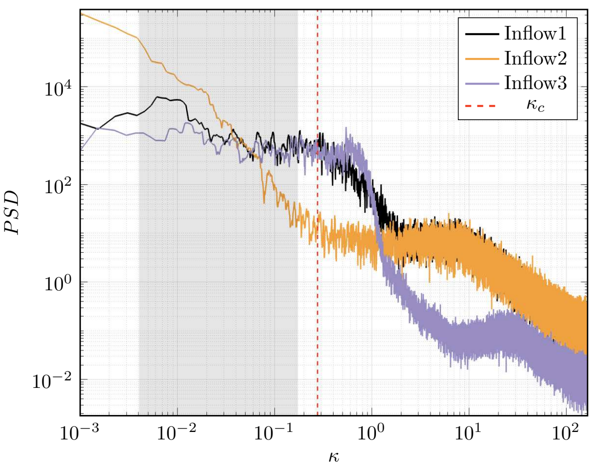

Figure 4: Power spectral density (PSD) of `Inflow1`, `Inflow2` and `Inflow3` vs reduced frequency. Shaded region represents the 1P reduced frequency range for a typical modern wind turbine blade. Also seen is the slat control reduced frequency κ_c.

ferent time scales are quite similar with heavy tails and exhibit non Gaussian characteristics. The corresponding shape factor in figure 5 (b) shows an increasing trend with increasing τ. It reaches the maximum value at $\tau = 0.015$ s, which means that the inflow displays largest intermittency levels at this time scale. Beyond $\tau = 0.015$ s the shape parameter reduces but still has significantly high values. The increment PDFs and λ^2 show that `Inflow1` has high levels of intermittent characteristics at smaller as well as larger time scales. Now focusing on inflow case `Inflow2`, the increment PDFs in figure 5 (c) show non Gaussian distribution for all the time scales. For $\tau = 0.673$ s the PDF is very heavy tailed towards the negative increment. The shape parameter distribution in figure 5 (d) shows a constant trend till approximately $\tau = 0.05$ s. A little drop is observed for higher time scales, but still maintaining high λ^2 values. When comparing this to the shape parameter for `Inflow1`, `Inflow2` exhibits higher values of λ^2 for time scales larger than $\tau = 0.02$ s. Thus, it can be inferred that this particular inflow has high intermittent characteristics at large time scales. The increment PDFs of inflow case `Inflow3` in figure 5 (e) shows Gaussian characteristics at all the scales, except the very small time scale of $\tau = 0.002$ s. This is very well reflected in the shape parameter distribution in figure 5 (f). The shape parameter has high values at the smallest time scales and sees a drastic negative gradient for higher values of τ. It quickly drops to values close to 0, reflecting Gaussian characteristics for large time scales.

As a quick summary of the discussion above, it can be inferred that `Inflow1` consists of high as well as low frequency fluctuations. Inflow case `Inflow2` on the other hand displays dominating low frequency fluctuations and has gust like characteristics. The third inflow case `Inflow3` has Gaussian characteristics for most relevant scales and shows intermittent nature only for very high frequency fluctuations.

IV. ACTIVE SLAT OPEN LOOP CONTROL

The definition and generation of complex inflow is followed by the creation of the slat trajectory through which the gap size of the active slat is controlled. The static characterization of the active slat has been done in the previous work done at University of Oldenburg[25]. It was found that the polar of the airfoil changes with the variation of gap size g_s between the leading edge slat and the main body of the airfoil (figure 6). Thus, in principle providing the ability to change the aerodynamic forces acting on the airfoil for the same angle of attack α. The open loop control leverages this property of the active slat in an attempt to reduce the fluctuating aerodynamic forces under the influence of complex inflow conditions.

Creation of the open loop control slat trajectory requires mainly two inputs, first being the static polar look up table and the second being the inflow angle time series. As mentioned in section III, the characterization of the inflow is done by using a X-type hot wire anemometer at the location of the airfoil in an empty wind tunnel. The presence of the airfoil in the wind tunnel would have some effects on the flow field. In order to take these effects into consideration for the development of the open loop control strategies, an indirect method is used to estimate the angle of attack of the inflow. The forces on

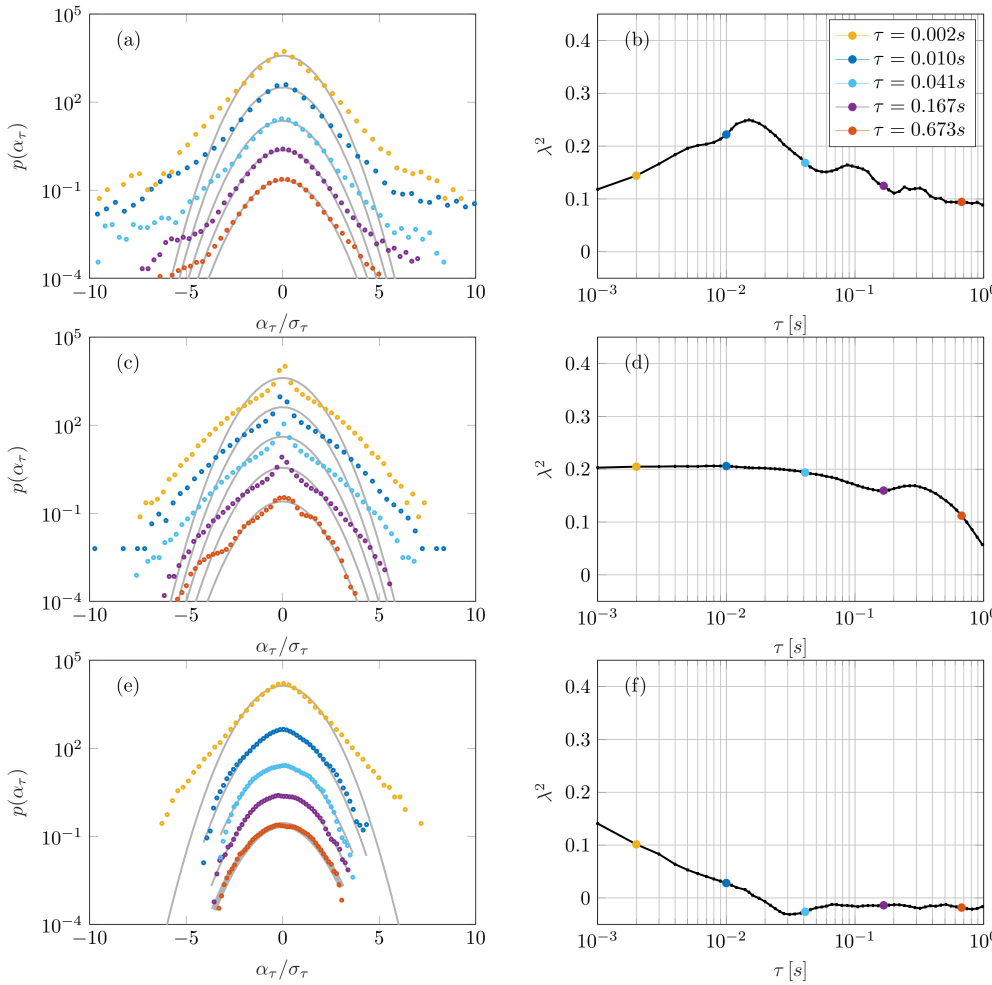

Figure 5: (a),(c), (e) show the PDF of velocity increments for `Inflow1`, `Inflow2` and `Inflow3` respectively. All graphs are vertically shifted against each other for clarity of presentation. The grey curves are respective Gaussian distribution fits. Subplots (b), (d) and (f) show the respective shape parameter λ^2 as a function of τ for `Inflow1`, `Inflow2` and `Inflow3`.

the airfoil vary with time under the influence of different inflow. At a time instance, the measured lift coefficient of the airfoil is obtained. Using the lift coefficient and the aerodynamic polar, the respective angle of attack at that particular time instance is estimated (figure 7). When this is done for all the time instances, we get the estimated angle of attack time series. The airfoil interacts with inflow structures of different scales in the wind tunnel. When we measure the forces we measure their average effect over the entire chord length of the airfoil. Inflow structures which are very small as compared to length scale of the airfoil get averaged out in the force measurements. This is why the extracted angle of attack using this indirect method mostly contains the the scales relevant to the airfoil. Leveraging the static polars for estimation of $\alpha\,(t)$ introduces a time delay due to the re-

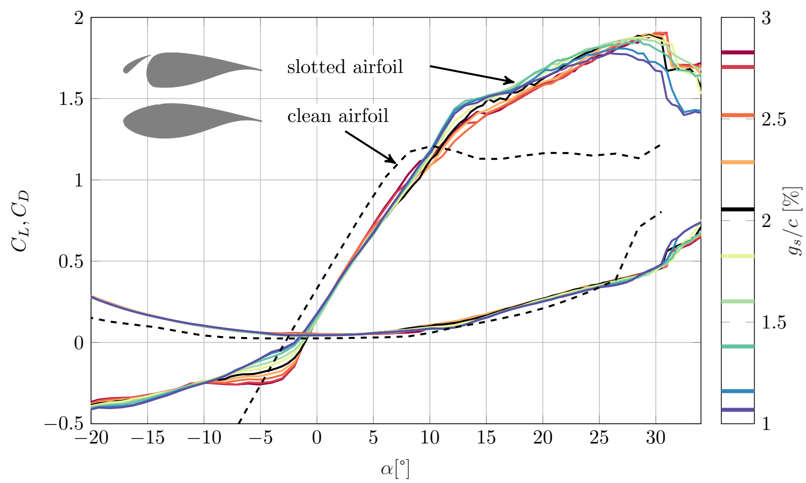

Figure 6: Static lift coefficients C_L and drag coefficients C_D for laminar inflow with $\mathrm{Re} = 0.6 \cdot 10^6$ for different gap sizes g_s compared to the clean airfoil without slat (adapted from Neuhaus et al.[25]).

sponse time of the airfoil to the dynamic inflow variation. Having this delay in the time series itself is beneficial for the slat control strategy, which can then be programmed without considering it further.

For applying this method to estimate the angle of attack time series $\alpha(t)$ for a complex inflow, first the forces on the airfoil are measured with the slat positioned at its reference gap size $g_{s,ref}$. The lift coefficient time series $C_L\left(t, g_{s,ref}\right)$ and the static polar for reference gap size $C_L\left(\alpha, g_{s,ref}\right)$ acts as the input for the determination of $\alpha(t)$. Now based on the static polar for all g_s and $\alpha(t)$, it is possible to compute C_L,C_D and C_M time series for all g_s. Based on different control protocols the variation of slat gap-size $g_s(t)$ with time is obtained. The control strategies can be designed in various ways to manipulate the loads as desired. The details about the different control strategies used are out of scope of the present article.

The gap size between the slat and mainbody of the airfoil is controlled using a stepper motor as described in section II. The gap size time series $g_s(t)$ needs to be translated into a control protocol which can be fed to the motor. The control protocol is basically a path for the stepper motor to follow. This path is not a continuous function but rather given in discrete steps with a certain temporal spacing defined by a control frequency f_c. This control frequeny can also be seen as the the frequency at which the active slat is controlled. In theory, a higher control frequency should result in better load control on the airfoil through manipulation of structures on a larger spectrum of scales. The control frequency however is limited by the torque provided by the stepper motor. The high frequency movement of the slat also causes the adverse effect of inducing structural vibration in the system. The slat control was tested at different frequencies and the optimum control frequency for the present scenario was found to be 8 Hz. The results discussed in the following section have the slat control frequency f_c of 8 Hz. The reduced frequency κ_c corresponding to the control frequency f_c of the active slat is indicated in figure 4. It is observed that κ_c is higher than the reduced frequencies experienced by a typical modern wind turbine. Thus the active slat should be able to influence loads having a wide range of unsteady characteristics.

V. RESULTS

The airfoil with the integrated active slat is exposed to the three complex inflows defined in section III. As stated in section III, for simulating the operating range of the angle of attack in a real world scenario, the airfoil is pitched to an angle of 10°. Thus the resultant angle of attack $\alpha_r(t)$ seen by the airfoil is the summation of inflow angle time series and the airfoil pitch angle. It is tested under two main cases: active slat and static slat. As the name suggests, in the active slat case the slat is actively controlled to vary the gap size between the slat and main body of the airfoil. This is done according to the designed slat control strategies. The main objective of the designed control strategies is to reduce the fluctuations of the control parameters while keeping the mean value constant. The static case on the other hand refers to the case where the gap size is fixed to $g_{s,ref}$. This case acts as the baseline case to which the active slat case is

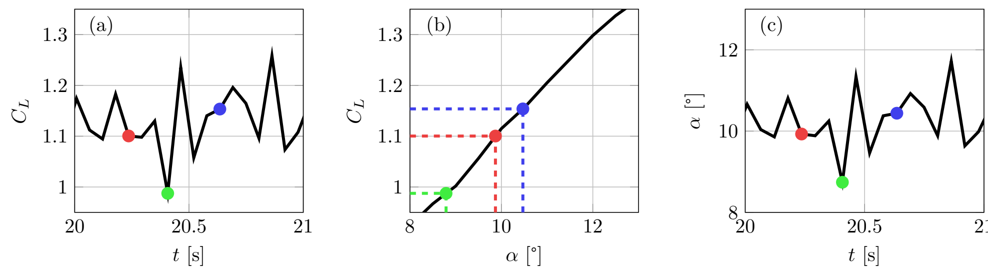

Figure 7: (a) Input C_L time series. (b) Corresponding values of α from the static polar. (c) Estimated angle of attack time series.

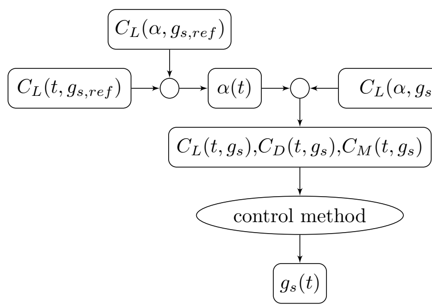

Figure 8: Slat trajectory creation algorithm

compared. While the open loop control was tested for many control parameters, the present article limits itself to the results of lift coefficient C_L as the control parameter. The control strategy used for the presented results aims to keep the C_L fluctuations as low as possible with respect to its mean value $\overline{C_L(t)}$. In this control strategy, for each time instance t_i the gap-size providing a C_L value closest to $\overline{C_L(t)}$ is chosen as $g_s(t_i)$. This is done for all the time instances to get the slat gap-size time series $g_s(t)$.

The effect on the lift coefficient by the airfoil's aerodynamic interaction with the defined inflows can be observed in figure 9. The figure presents a comparison of the static slat and active slat cases. The control parameter which is used for creation of the control strategy in this case is the lift coefficient. The comparison for the `Inflow1` case in figure 9 (a) indicates a slight reduction in fluctuations of the lift coefficient for the active slat. When inspecting the `Inflow2` case, a significant reduction in C_L fluctuation can be observed in the active slat case. On the other hand the `Inflow3` case does not show any observable reduction in C_L fluctuation.

To get a more quantitative perspective, the values of the mean and standard deviation of the C_L time series for active and static slat is presented in table I. It is observed that for `Inflow1` the active slat is able to reduce the standard deviation of the lift coefficient time series by almost 10 %. The mean value on the other hand remains almost the same for both the cases. The active slat is most effective in mitigating the lift coefficient for the `Inflow2`, where a reduction in standard deviation of approximately 59 % is observed. For this inflow, the control strategy is able to mitigate the fluctuations caused by the gust like effects in the inflow. The mean lift coefficients though shows an increase of 1.7 %. The active slat is able to mitigate most of the gust like C_L fluctuations because they are created by structures with large time scales.

The active slat case seems to be ineffective in C_L fluctuation reduction for the `Inflow3`, rather it amplifies the fluctuation by almost 19 %. The control strategy used is optimised to handle significant structures in the inflow as one would expect natural flows to have. The fluctuations due to `Inflow3` are very difficult to control because the inflow has no structures in scales which can be actively manipulated by the slat. Perhaps a different control strategy needs to be adapted to handle flows with white noise characteristics.

Table I: Comparison of C_L mean and standard deviation for the static and active slat.

Inflow	Static Slat		Active Slat		Change [%]	
	$\overline{C_L}$	σ_{C_L}	$\overline{C_L}$	σ_{C_L}	$\overline{C_L}$	σ_{C_L}
`Inflow1`	1.105	0.050	1.103	0.045	-0.14	-10
`Inflow2`	1.165	0.054	1.184	0.022	1.7	-59
`Inflow3`	1.103	0.034	1.125	0.040	1.9	19

Control of one coefficient (in this case C_L) does not necessarily mean that the total forces on the airfoil are reduced. Positive outcome of the control can only be fully judged when other coefficients are examined as well. This is very important because reducing fluctuations of one coefficient can very well result in amplification of others. Also it is essential to take into account the weighted influence of the reduction or amplification of each coefficient. For this comparative study, two approaches discussed below are being used to analyse the results further.

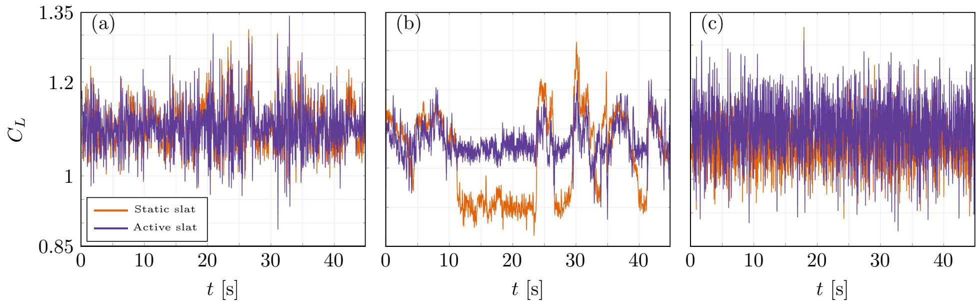

Figure 9: Lift coefficient C_L time series comparison of the active slat (purple) and static slat with $g_s = gs, ref$ (orange) , for the inflow cases `Inflow1` (a), `Inflow2` (b) and Inflow3 (c).

A. Cumulative standard deviation comparison

We define a parameter,

$$\sigma_r = \sqrt{\int_0^{f_r} \frac{S(f)}{f_r} df} \tag{4}$$

which represents cumulative standard deviation. It is defined as the standard deviation of sum of all the components of a time series within the frequency range 0 to f_r (equation (4)). Here S is the power spectral density of the time series. σ_r gives an indication of the contribution of fluctuation of different time scales in the time series. Hence the standard deviation of the full time series is equal to the cumulative standard deviation when f_r is equal to the sampling frequency of the measurement.

Based on the definition of σ_r, the cumulative standard deviation is computed for both the active and static slat case for various values of f_r. These have been named as $\sigma_{r_{active}}$ and $\sigma_{r_{static}}$ for the respective cases. The difference of the cumulative standard deviation for the active and static cases ($\sigma_{r_{active}} - \sigma_{r_{static}}$) is plotted with respect to f_r in figure 10. A negative value of ($\sigma_{r_{active}} - \sigma_{r_{static}}$) indicates at lower fluctuation in the active slat case as compared to the static one. On the other hand, a positive ($\sigma_{r_{active}} - \sigma_{r_{static}}$) indicates that the active slat is causing amplification of fluctuation as compared to that of the static slat.

Figure 10 presents the difference of the cumulative standard deviation for the static and active slat cases for `Inflow1`, `Inflow2` and `Inflow3`. Although the control parameter for the present control strategy is the lift coefficient C_L, the drag C_D and moment coefficient C_M are plotted for comparison as well. This enables us to understand the effect on the drag and moment penalty when controlling C_L. It is observed that for the `Inflow1` and `Inflow2` cases the C_L fluctuation is significantly reduced as compared to slight amplification of C_D and C_M. Thus this indicates that the drag penalty is significantly lower as compared to the gains in the mitigation of lift coefficient. `Inflow3` does not show any such trends and the difference in the fluctuation of active and static slat cases is negligible for all the coefficients.

B. Flapwise and edgewise components of lift and drag.

Although the lift force fluctuation gives a good indication of the fatigue loading on the blade, a direct look at the resolved forces of lift and drag in the rotational plane and the normal plane can give further insight. This will give the resultant contribution of both the lift and drag forces acting on the airfoil. The forces in the rotational plane of the blade contributes to the edgewise force while the one in the normal plane is part of the flapwise force.

We define the component of the aerodynamic forces (lift force L and drag force D) in the flapwise force direction as F_f while the component in the edgewise direction is defined as F_e (figure 11). The time series for F_f and F_e can be computed using the measured lift L and drag D time series and the total angle of attack time series $A(t)$. The total angle of attack $A(t)$ comprises of the resultant angle of attack $\alpha_r(t)$ and geometrical angle θ. The geometrical angle comprises of the twist and pitch angle of the airfoil. For the present calculations θ has been set to 10°.

$$A(t) = \alpha_r(t) + \theta \tag{5}$$

$$F_f(t) = Lcos(A(t)) + Dsin(A(t)) \tag{6}$$

$$F_e(t) = Lsin(A(t)) - Dcos(A(t)) \tag{7}$$

The respective flapwise and edgewise force coefficients are termed as C_f and C_e. They can be obtained by

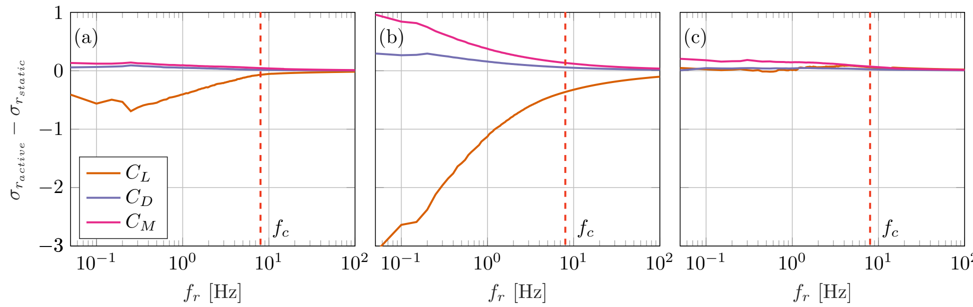

Figure 10: Difference of cumulative standard deviation of static slat $\sigma_{r_{static}}$ from active slat $\sigma_{r_{active}}$ vs f_r for the lift coefficient C_L, drag coefficient C_D and moment coefficient C_M. Subplots (a), (b), (c) present the inflow cases `Inflow1`, `Inflow2` and `Inflow3` respectively.

dividing equations 6 and 7 with $(q \cdot c \cdot s)$, where q is the dynamic pressure, c is the airfoil chord and s is the airfoil span.

$$C_f(t) = C_L cos(A(t)) + C_D sin(A(t)) \tag{8}$$

$$C_e(t) = C_L sin(A(t)) - C_D cos(A(t)) \tag{9}$$

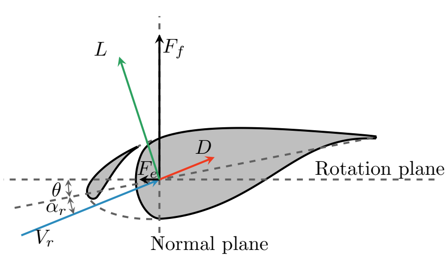

Figure 11: Forces acting on a wind turbine blade section

The resolved force coefficients are computed for the active and static slat cases, for each of the inflow cases defined in section III. The comparison of the active and static slat case for `Inflow1` is presented in figure 12, where sub-figure 12 (a) presents the C_f time series comparison while sub-figure 12 (b) presents C_e time series comparison. Visually a slight reduction in the fluctuation is observed in the active slat case for both the components. Sub-figures 12 (c) and(d) present the respective comparison for `Inflow2`. Here, in both C_f and C_e time series a drastic reduction of fluctuation is observed for the active slat case.

Table II: Comparison of mean and standard deviation of the flapwise components of C_L and C_D time series for the static and active slat.

Inflow	Static Slat		Active Slat		Change [%]	
	$\overline{C_f}$	σ_{C_f}	$\overline{C_f}$	σ_{C_f}	$\overline{C_f}$	σ_{C_f}
`Inflow1`	1.106	0.048	1.104	0.043	-0.18	-10.4
`Inflow2`	1.166	0.052	1.184	0.022	1.54	-57.69
`Inflow3`	1.105	0.032	1.125	0.039	1.81	21.87

Table III: Comparison of mean and standard deviation of the edgewise components of C_L and C_D time series for the static and active slat.

Inflow	Static Slat		Active Slat		Change [%]	
	$\overline{C_e}$	σ_{C_e}	$\overline{C_e}$	σ_{C_e}	$\overline{C_e}$	σ_{C_e}
`Inflow1`	0.088	0.026	0.089	0.023	1.14	-11.53
`Inflow2`	0.087	0.039	0.099	0.033	13.79	-15.38
`Inflow3`	0.087	0.018	0.099	0.02	13.79	11.11

The C_f and C_e mean values and standard deviations of the active and static slat cases are presented in table II and table III respectively. The tables present the data for each of the three turbulent inflow cases. For `Inflow1` the active slat case is able to reduce the standard deviation of flapwise component of load fluctuation by 10.4 %, while for the edgewise component the reduction is noted to be 11.5 %. For `Inflow2` the active slat decreases the fluctuating loads by 57.7 % for C_f and 15.4 % C_e. The active slat does not mitigate the loads for the third inflow case i.e `Inflow3`. Here an amplification of the loads is observed, 21.9 % for C_f and approximately 11.1 % C_e. The load reduction with the help of the active slat in the edgewise direction is far less than that observed in the flapwise direction. It is important to remember that the

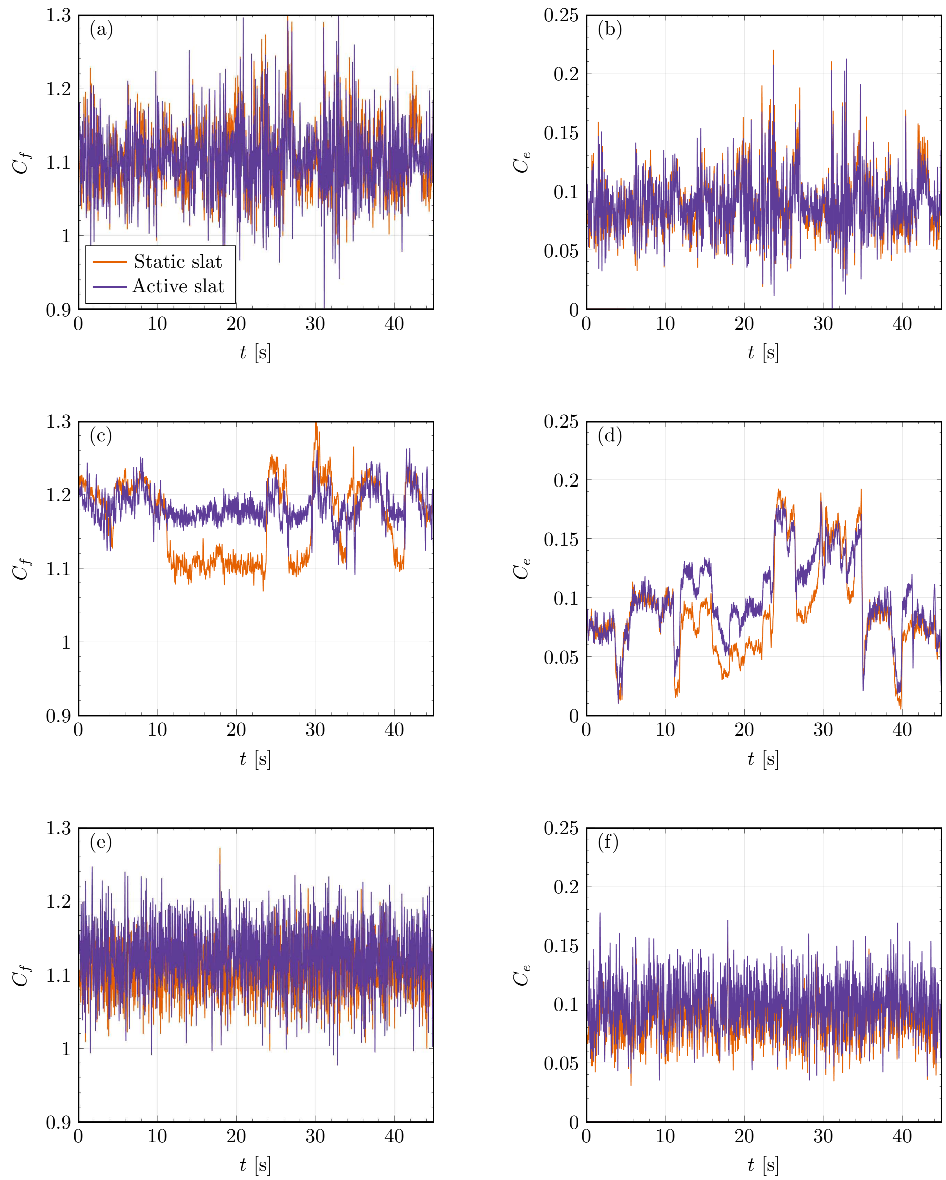

Figure 12: Subfigure(a),(c) and (e) are the C_f time series for the inflow cases `Inflow1`,`Inflow2` and `Inflow3`. Subfigure (b),(d) and (f) are the C_e time series for the inflow cases `Inflow1`,`Inflow2` and `Inflow3`. Each subfigure presents comparison of the active slat (purple) and static slat with $g_s = gs, ref$ (orange)

.

turbulence induced fatigue loads play a very significant role in the flapwise cyclic loads while the edgewise loads are dominated by gravitational forces[6]. The reduction of turbulence induced loads in the flapwise direction is more important from the perspective of the overall load reduction on a wind turbine blade.

VI. CONCLUSION

An actively deformable integrated slat concept on a DU91-W2-250 airfoil was comprehensively tested for mitigation of fluctuating loads on the airfoil. The aerodynamic forces acting on the airfoil can be manipulated by changing the gap size between the slat and main body of the airfoil. To extensively test the active slat system, three distinct complex inflow conditions of varying levels of intermittency were generated. Inflow case `Inflow1` has significant presence of fluctuation at large as well as small time scales. On the other hand `Inflow2` has dominant presence of low frequency gust like features, while `Inflow3` has Gaussian characteristics on large scales and high intermittency on small scales. The distinct features of the inflows ensures that the operation of the active slat is investigated under a wide spectrum of loads.

Different open loop control strategies were developed to reduce the fluctuations of the desired control parameter by keeping the variation of its mean value to the minimum. The present article limits itself to the discussion of the control parameter lift coefficient. The airfoil was exposed to the three inflows and the slat was actively controlled for load mitigation and this case was termed as the active slat case. The active slat measured load was compared to the static slat case, where the slat is fixed with reference gap size. For the inflow case `Inflow1` the active slat was able to reduce the standard deviation of the lift coefficient by 10 %. The active slat reduced the fluctuating lift coefficient for `Inflow2` by an astounding 59 %. It successfully mitigated the load fluctuations caused by the low frequency gust characteristics of the inflow. For `Inflow3` however, the active slat was ineffective and rather amplified the lift coefficient fluctuation by 19 %. This might be because the control strategy was optimised to handle defined structures in the inflow and `Inflow3` is devoid of those at the scales controlled by the slat. For all the three inflow cases, the mean value variation was kept below 2 %. The effect of the active slat on loads other than the control parameter C_L was investigated by using the cumulative standard deviation. A small drag and moment penalty was observed for inflow cases `Inflow1` and `Inflow2`, but the gains obtained by lift fluctuation mitigation were found to be much more significant. The effect of the active slat on the loads in the rotational and normal planes of a wind turbine rotor blade was examined by resolving the lift and drag forces on the airfoil in edgewise and flapwise directions. When exposed to `Inflow1`, the active slat alleviated approximately 10 % and 5 % fluctuations for flapwise and edgewise loads respectively. For inflow case `Inflow2` the active slat caused reductions of approximately 58 % flapwise and 15 % edgewise load fluctuations. It is ineffective in reducing the load fluctuations for `Inflow3`.

The experimental investigation of the active slat concept demonstrates the potential of the concept for mitigating unsteady loads on an airfoil. The active slat is able to alleviate load fluctuations over a wide spectrum of unsteady loads, but it is most effective in mitigating low frequency gust like loads. It proves to be an important initial step for the development of a promising active flow control device for addressing the issues of energy loss due to flow separation and high fatigue load in the inboard region of a wind turbine blade. The transition from the proof of concept on a two dimensional airfoil to its application on a three dimensional blade brings some challenges which need further research. The reduction of the complexity of the system is one such challenge. Other aspect that needs further research is the aeroacoustic noise generated from the slat. The current study was based on an open loop control strategy and relies on good quality inflow data. Closed loop control strategies or a combination of open and closed loop control strategies need to be explored to make the active slat system more robust for real world operational conditions.

ACKNOWLEDGMENTS

This work has been funded by the German Ministry of Economic Affairs and Energy (BMWi) on decision of the German Parliament in the frame of the SmartBlades 2.0 project (funding reference no. 0324032A/D). The authors gratefully acknowledge the German Ministry of Economic Affairs and Energy for funding this work. The authors are also thankful to the learned referees for their valuable constructive suggestions which has helped in improving this article.

DATA AVAILABILITY

Raw data were generated in the wind tunnel at the university of Oldenburg. Derived data supporting the findings of this study are available from the corresponding author upon reasonable request.

REFERENCES

[1] M. Wächter, H. Heißelmann, M. Hölling, A. Morales, P. Milan, T. Mücke, J. Peinke, N. Reinke, and P. Rinn, "The turbulent nature of the atmospheric boundary layer and its impact on the wind energy conversion process," Journal of Turbulence **13**, N26 (2012).

[2] M. Hölling, J. Peinke, and S. Ivanell, *Wind energy-Impact of turbulence*, Vol. 2 (2014).

[3] S. Lee, M. J. Churchfield, P. J. Moriarty, J. Jonkman, and J. Michalakes, "A numerical study of atmospheric and wake tur-

bulence impacts on wind turbine fatigue loadings," Journal of Solar Energy Engineering **135** (2013).

[4] A. Lavely, G. Vijayakumar, M. Kinzel, J. Brasseur, and E. Paterson, "Space-time loadings on wind turbine blades driven by atmospheric boundary layer turbulence," in *49th AIAA Aerospace Sciences Meeting including the New Horizons Forum and Aerospace Exposition* (2011).

[5] B. Ernst and J. R. Seume, "Investigation of site-specific wind field parameters and their effect on loads of offshore wind turbines," Energies **5**, 3835–3855 (2012).

[6] A. Rezaeiha, R. Pereira, and M. Kotsonis, "Fluctuations of angle of attack and lift coefficient and the resultant fatigue loads for a large horizontal axis wind turbine," Renewable Energy **114**, 904–916 (2017).

[7] F. Spinato, P. J. Tavner, G. J. W. Van Bussel, and E. Koutoulakos, "Reliability of wind turbine subassemblies," IET Renewable Power Generation **3**, 387–401 (2009).

[8] B. L. Jones, W. H. Lio, and J. A. Rossiter, "Overcoming fundamental limitations of wind turbine individual blade pitch control with inflow sensors," Wind Energy **21**, 922–936 (2018).

[9] C. L. Bottasso, A. Croce, C. E. D. Riboldi, and M. Salvetti, "Cyclic pitch control for the reduction of ultimate loads on wind turbines," Journal of Physics: Conference Series **524**, 012063 (2014).

[10] I. Aramendia, U. Fernandez-Gamiz, J. A. Ramos-Hernanz, J. Sancho, J. M. Lopez-Guede, and E. Zulueta, "Flow control devices for wind turbines," Energy Harvesting and Energy Efficiency , 629–655 (2017).

[11] T. K. Barlas and G. A. M. van Kuik, "Review of state of the art in smart rotor control research for wind turbines," Progress in Aerospace Sciences **46**, 1–27 (2010).

[12] C. P. Van Dam, D. E. Berg, and S. J. Johnson, "Active load control techniques for wind turbines," Tech. Rep. (Sandia National Laboratories, 2008).

[13] S. J. Johnson, J. P. Baker, C. P. Van Dam, and D. Berg, "An overview of active load control techniques for wind turbines with an emphasis on microtabs," Wind Energy **13**, 239–253 (2010).

[14] P. B. Andersen, L. Henriksen, M. Gaunaa, C. Bak, and T. Buhl, "Deformable trailing edge flaps for modern megawatt wind turbine controllers using strain gauge sensors," Wind Energy **13**, 193–206 (2010).

[15] W. Zhang, Y. Wang, R. Liu, H. Liu, and X. Zhang, "Unsteady aerodynamic modeling and control of the wind turbine with trailing edge flap," Journal of Renewable and Sustainable Energy **10**, 063304 (2018).

[16] X. Bofeng, F. Junheng, L. Qing, X. Chang, Z. Zhenzhou, and Y. Yue, "Aerodynamic performance analysis of a trailing-edge flap for wind turbines," Journal of Physics: Conference Series **1037**, 022020 (2018).

[17] I. Herráez, B. Akay, G. J. W. van Bussel, J. Peinke, and B. Stoevesandt, "Detailed analysis of the blade root flow of a horizontal axis wind turbine," Wind Energy Science **1**, 89–100 (2016).

[18] L. Gao, H. Zhang, Y. Liu, and S. Han, "Effects of vortex generators on a blunt trailing-edge airfoil for wind turbines," Renewable Energy **76**, 303–311 (2015).

[19] N. Troldborg, F. Zahle, and N. N. Sørensen, "Simulations of wind turbine rotor with vortex generators," Journal of Physics: Conference Series **753**, 022057 (2016).

[20] G. Pechlivanoglou, C. N. Nayeri, and C. O. Paschereit, "Fixed leading edge auxiliary wing as a performance increasing device for hawt blades," DEWEK, Bremen, Germany (2010).

[21] F. Zahle, M. Gaunaa, N. N. Sørensen, and C. Bak, "Design and wind tunnel testing of a thick, multi-element high-lift airfoil," in *Proceedings of EWEA 2012 - European Wind Energy Conference and Exhibition European Wind Energy Association (EWEA)* (2012).

[22] M. Gaunaa, F. Zahle, N. N. Sørensen, and C. Bak, "Quantification of the effects of using slats on the inner part of a 10 MW rotor," in *European Wind Energy Conference* (2012).

[23] A. M. O. Smith, "High-lift aerodynamics," Journal of Aircraft **12**, 501–530 (1975).

[24] D. N. Foster, "Flow around wing sections with high-lift devices," Journal of Aircraft **9**, 205–210 (1972).

[25] L. Neuhaus, P. Singh, T. Homeyer, O. Huxdorf, J. Riemenschneider, J. Wild, J. Peinke, and M. Hölling, "Mitigating loads by means of an active slat," Journal of Physics: Conference Series **1037**, 022032 (2018).

[26] P. Knebel, A. Kittel, and J. Peinke, "Atmospheric wind field conditions generated by active grids," Experiments in fluids **51**, 471–481 (2011).

[27] L. Kröger, J. Frederik, J. W. van Wingerden, J. Peinke, and M. Hölling, "Generation of user defined turbulent inflow conditions by an active grid for validation experiments," Journal of Physics: Conference Series **1037**, 052002 (2018).

[28] L. Kröger, L. Neuhaus, J. Peinke, G. Gülker, and M. Hölling, "Turbulence generation by active grids," in *Progress in Turbulence VIII* (2019).

[29] H. Heißelmann, J. Peinke, and M. Hölling, "Experimental airfoil characterization under tailored turbulent conditions," Journal of Physics: Conference Series **753**, 072020 (2016).

[30] T. T. B. Wester, J. Krauss, L. Neuhaus, A. Hölling, G. Gülker, M. Hölling, and J. Peinke, "How to design a 2D active grid for dynamic inflow modulation," arXiv preprint arXiv:2012.10245 (2020).

[31] A. Manso Jaume and J. Wild, "Aerodynamic design and optimization of a high-lift device for a wind turbine airfoil," New Results in Numerical and Experimental Fluid Mechanics X , 859–869 (2016).

[32] O. Huxdorf, J. Riemenschneider, P. Lorsch, and M. Radestock, "Structural design and experimental investigations of a shape-adaptive slat for wind energy rotor blades," in *SMART2017-8th ECCOMAS Thematic Conference on Smart Structures and Materials* (2017).

[33] C. M. Schwarz, S. Ehrich, R. Martin, and J. Peinke, "Fatigue load estimations of intermittent wind dynamics based on a blade element momentum method," Journal of Physics: Conference Series **1037**, 072040 (2018).

[34] C. M. Schwarz, S. Ehrich, and J. Peinke, "Wind turbine load dynamics in the context of turbulence intermittency," Wind Energy Science **4**, 581–594 (2019).

[35] J. Jonkman, S. Butterfield, W. Musial, and G. Scott, "Definition of a 5-MW reference wind turbine for offshore system development," Tech. Rep. (National Renewable Energy Lab.(NREL), Golden, CO (United States), 2009).

[36] G. Pereira, R.and Schepers and M. D. Pavel, "Validation of the Beddoes–Leishman dynamic stall model for horizontal axis wind turbines using MEXICO data," Wind Energy **16**, 207–219 (2013).

[37] C. Bak, F. Zahle, R. Bitsche, T. Kim, A. Yde, L. C. Henriksen, M. H. Hansen, J. P. A. A. Blasques, M. Gaunaa, and A. Natarajan, "The DTU 10-MW reference wind turbine," in *Danish Wind Power Research* (2013).

[38] J. Leishman, *Principles of Helicopter Aerodynamics*, Cambridge Aerospace Series (Cambridge University Press, 2016).

[39] B. Castaing, Y. Gagne, and E. J. Hopfinger, "Velocity probability density functions of high Reynolds number turbulence," Physica D: Nonlinear Phenomena **46**, 177–200 (1990).

[40] A. Morales, M. Wächter, and J. Peinke, "Characterization of wind turbulence by higher-order statistics," Wind Energy **15**, 391–406 (2012).

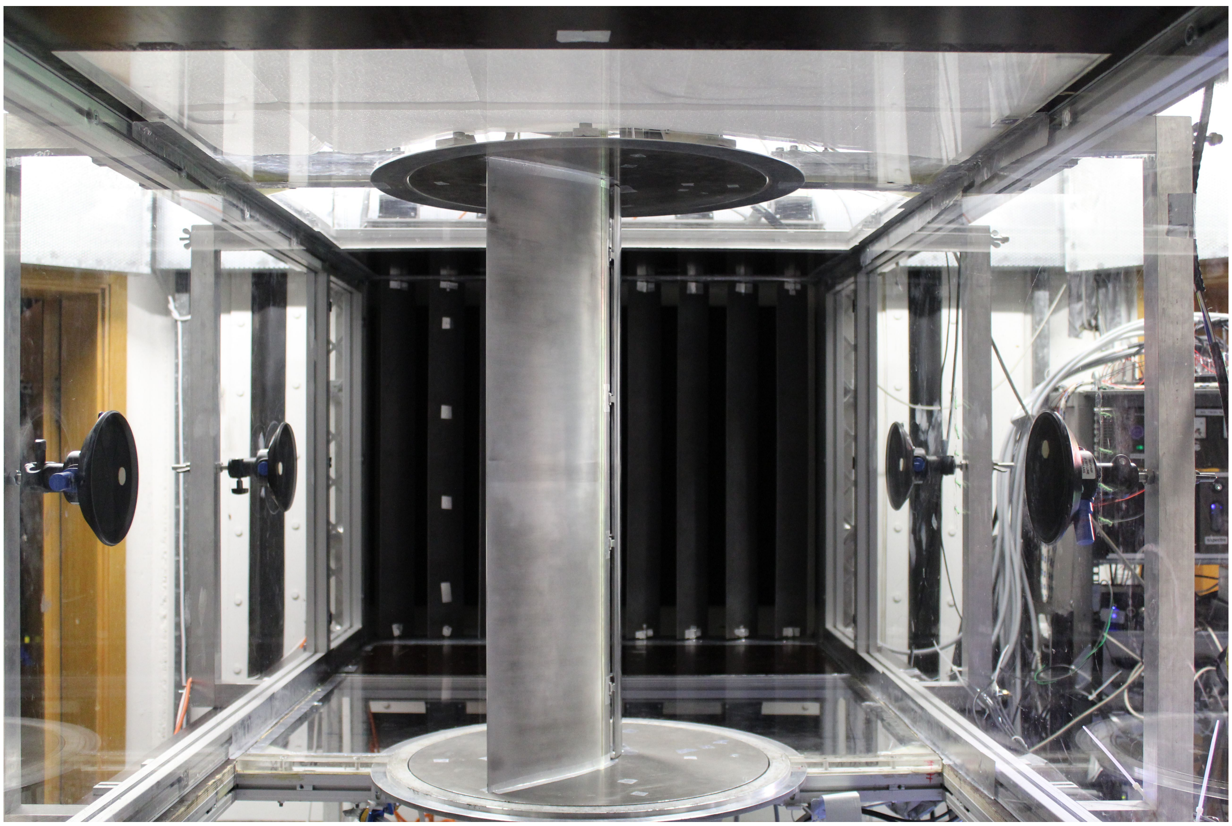

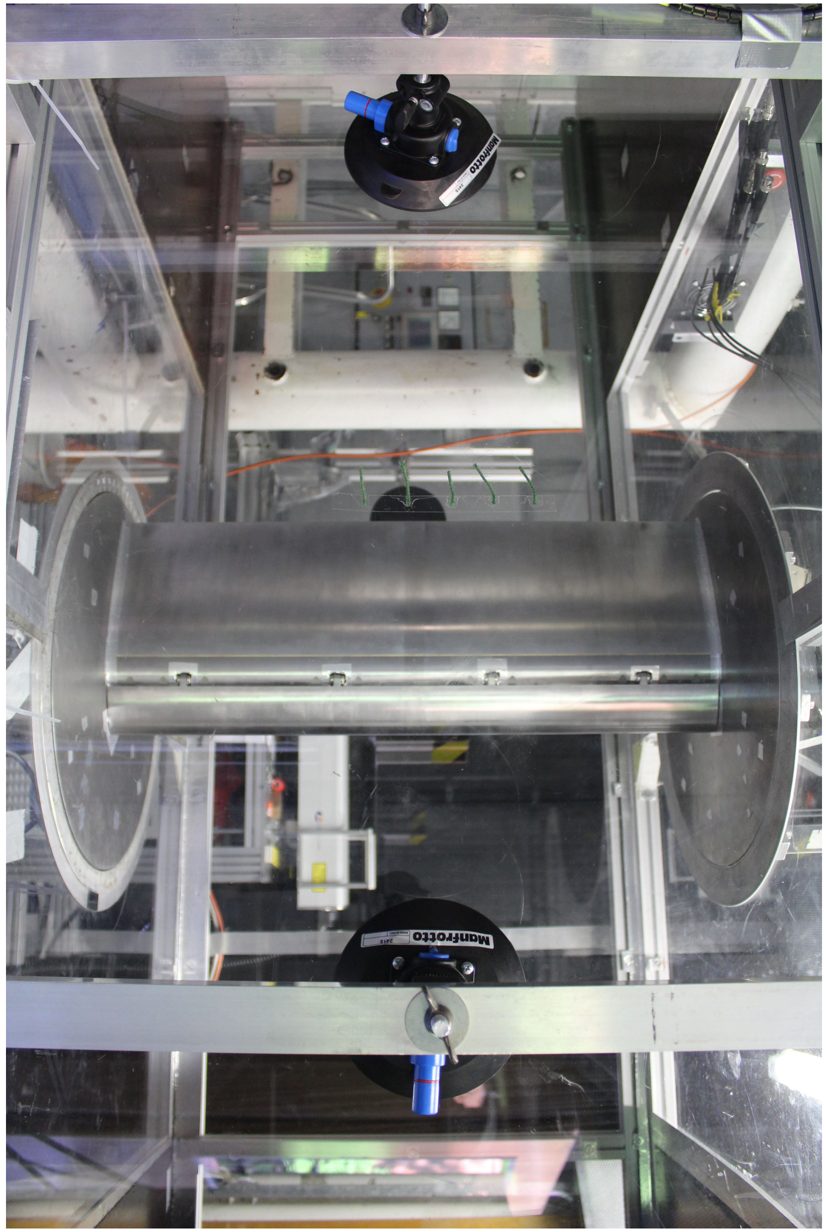
Manfrotto
Manfrotto

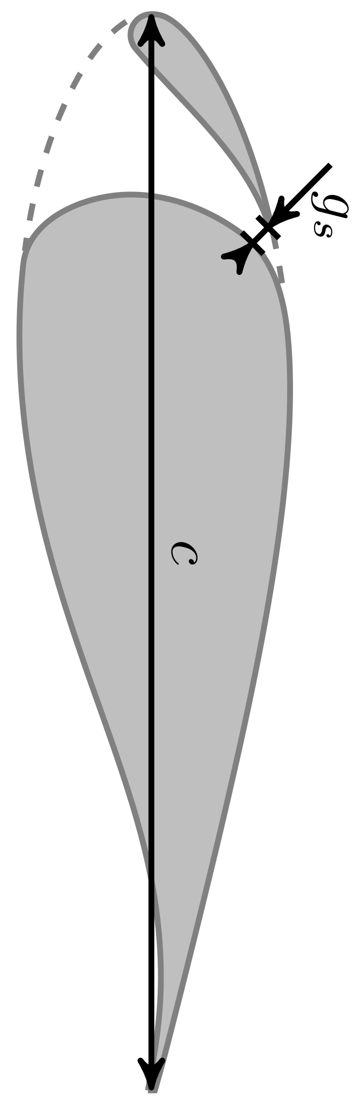
g_s
c

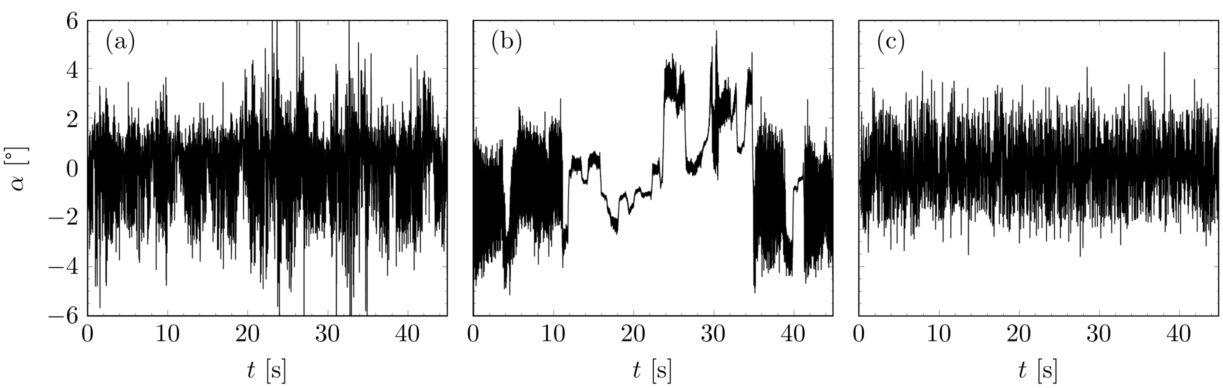
(a)
(b)
(c)
α [°]
t [s]
6
4
2
0
−2
−4
−6
0
10
20
30
40

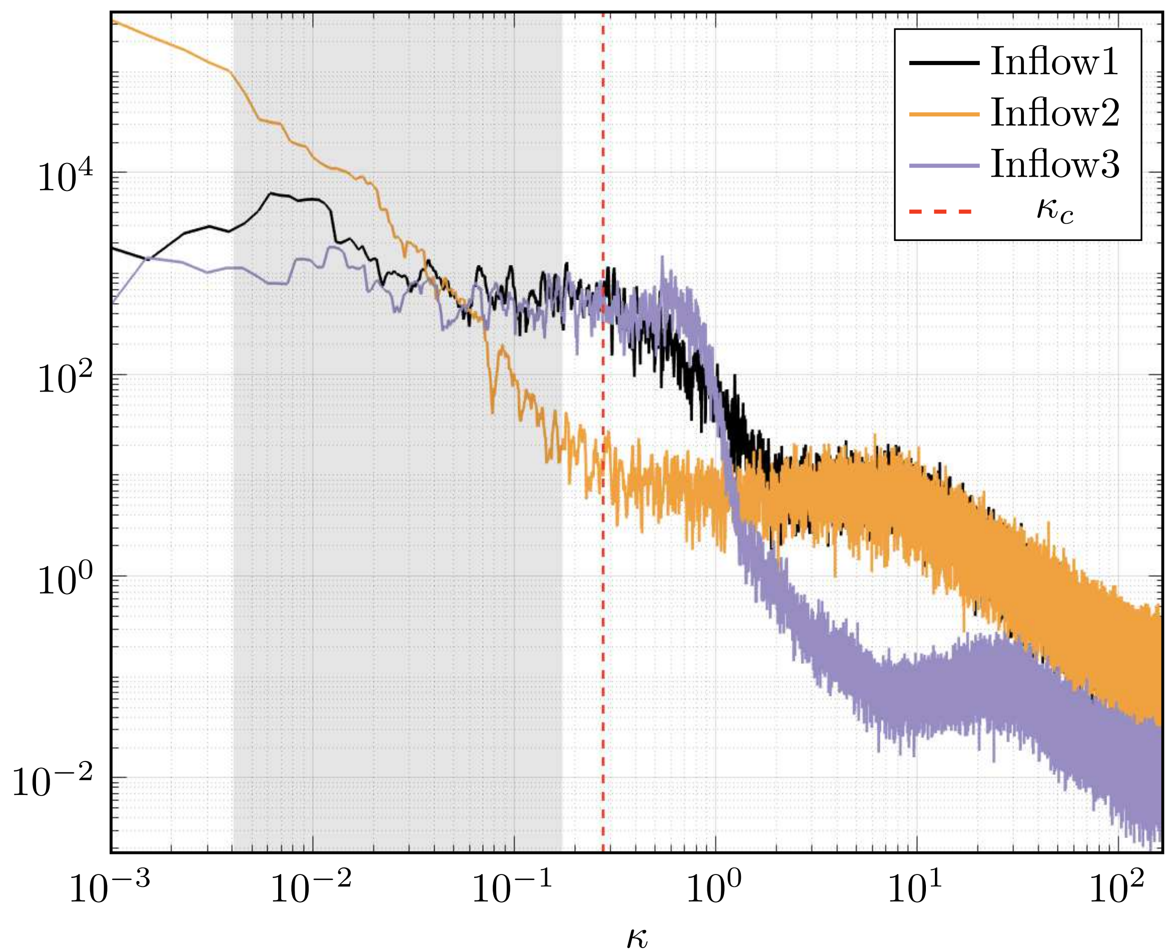
Inflow1
Inflow2
Inflow3
κ_c
PSD
κ
10^{4}
10^{2}
10^{0}
10^{-2}
10^{-3}
10^{-2}
10^{-1}
10^{0}
10^{1}
10^{2}

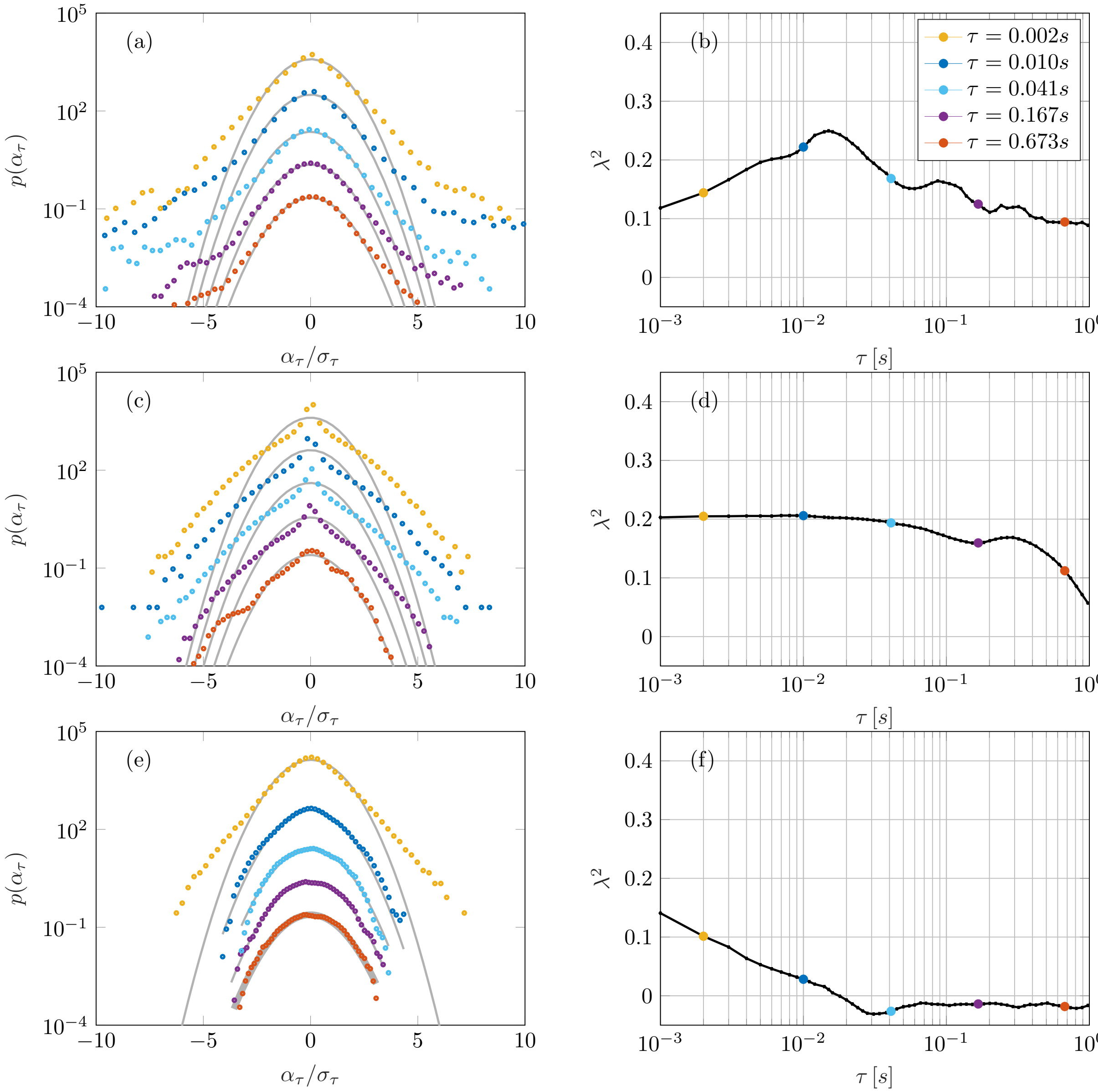
(a)
(b)
(c)
(d)
(e)
(f)
$p(\alpha_\tau)$
α_τ/σ_τ
λ^2
$\tau\,[s]$
$\tau = 0.002s$
$\tau = 0.010s$
$\tau = 0.041s$
$\tau = 0.167s$
$\tau = 0.673s$

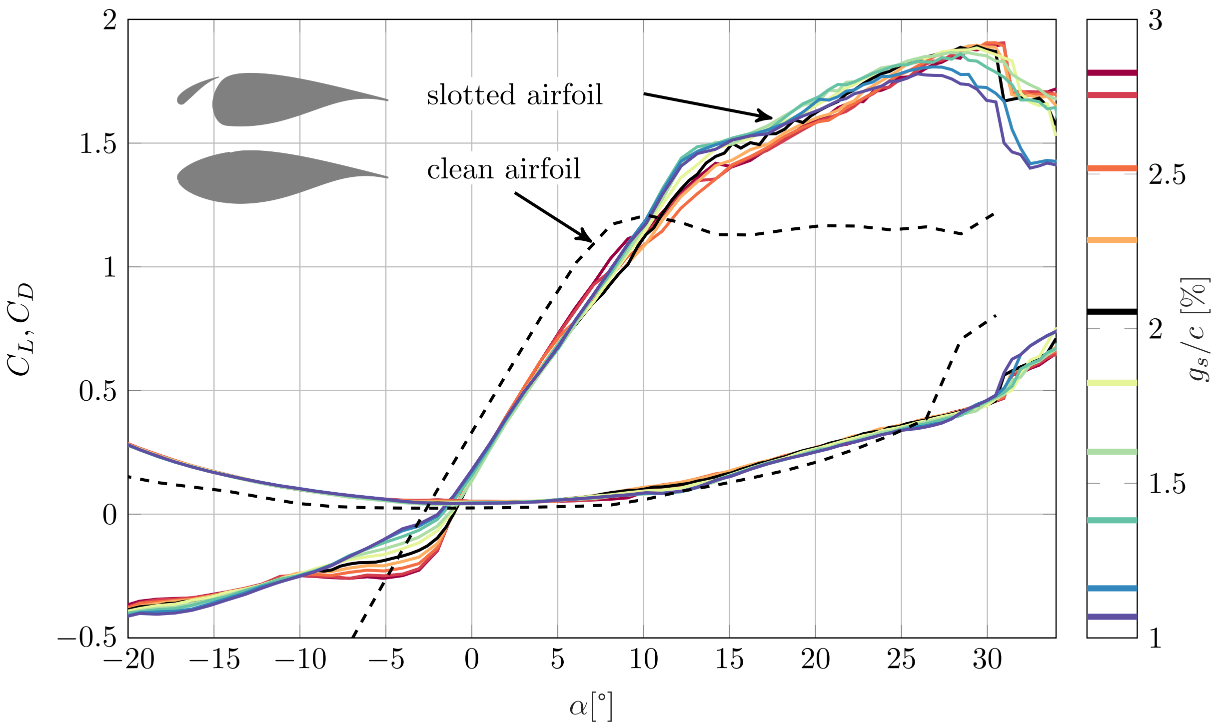
slotted airfoil
clean airfoil
C_L, C_D
$\alpha[°]$
g_s/c [%]
−20
−15
−10
−5
0
5
10
15
20
25
30
−0.5
0
0.5
1
1.5
2
2.5
3

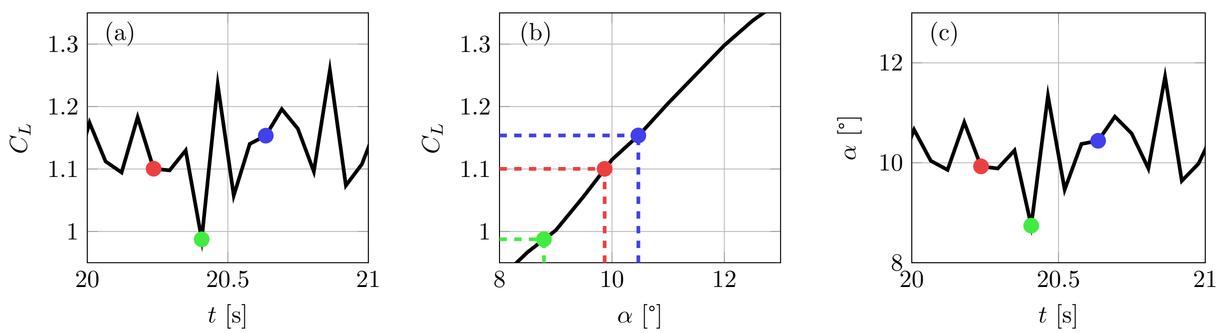
(a)
1.3
1.2
1.1
1
C_L
20
20.5
21
t [s]
(b)
1.3
1.2
1.1
1
C_L
8
10
12
α [°]
(c)
12
10
8
α [°]
20
20.5
21
t [s]

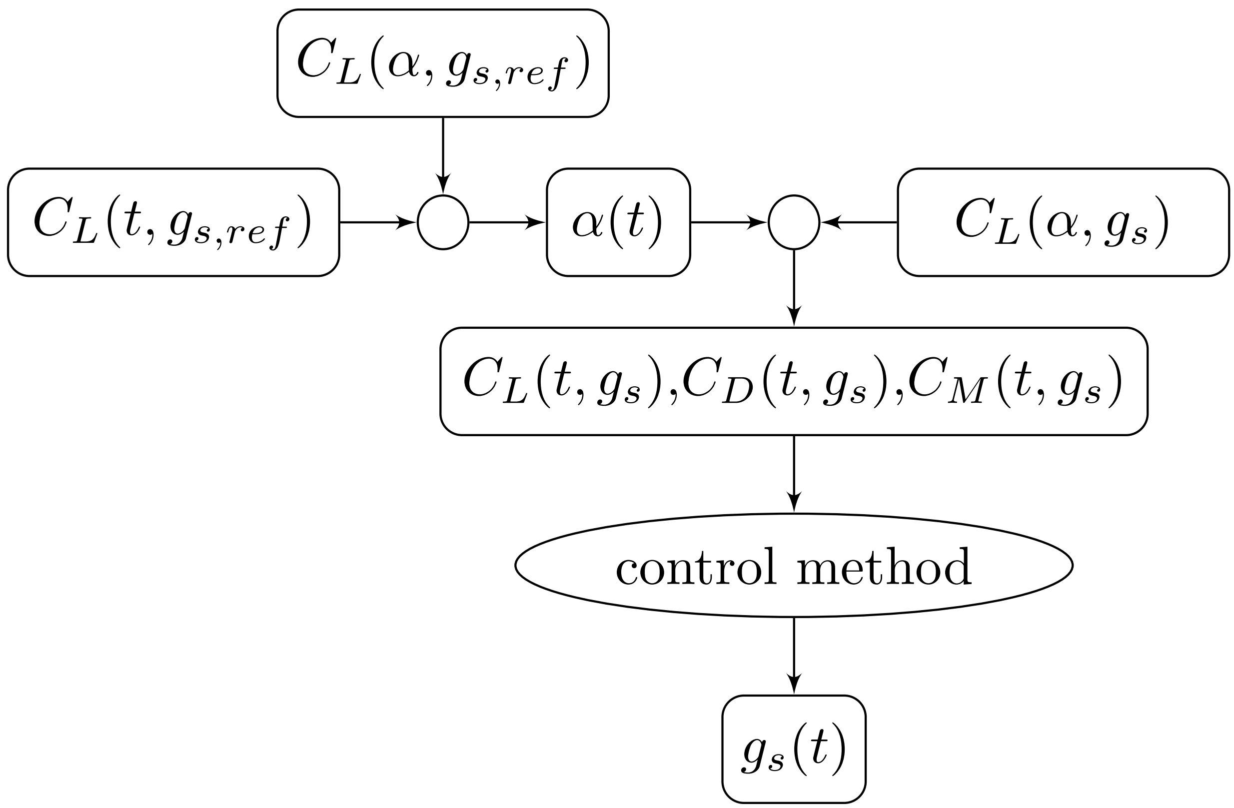
$C_L(\alpha, g_{s,ref})$
$C_L(t, g_{s,ref})$
$\alpha(t)$
$C_L(\alpha, g_s)$
$C_L(t, g_s)$,$C_D(t, g_s)$,$C_M(t, g_s)$
control method
$g_s(t)$

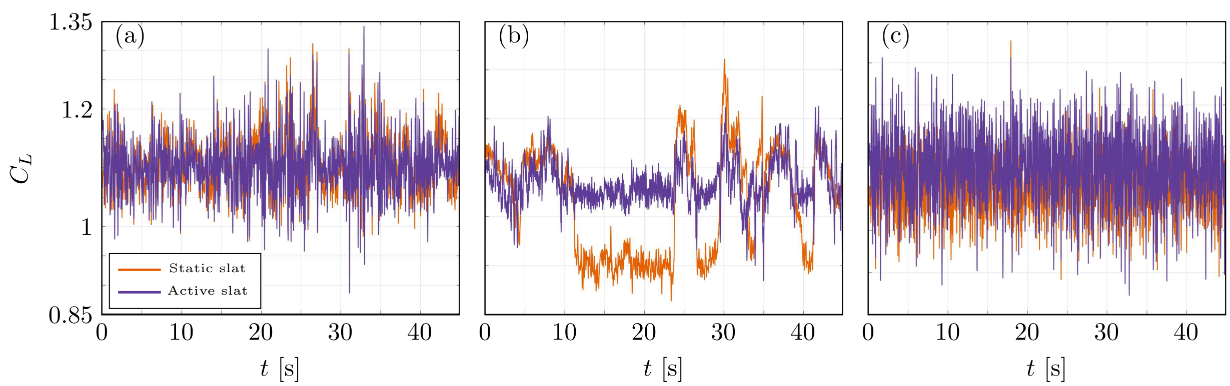
(a)
(b)
(c)
C_L
1.35
1.2
1
0.85
0
10
20
30
40
t [s]
Static slat
Active slat

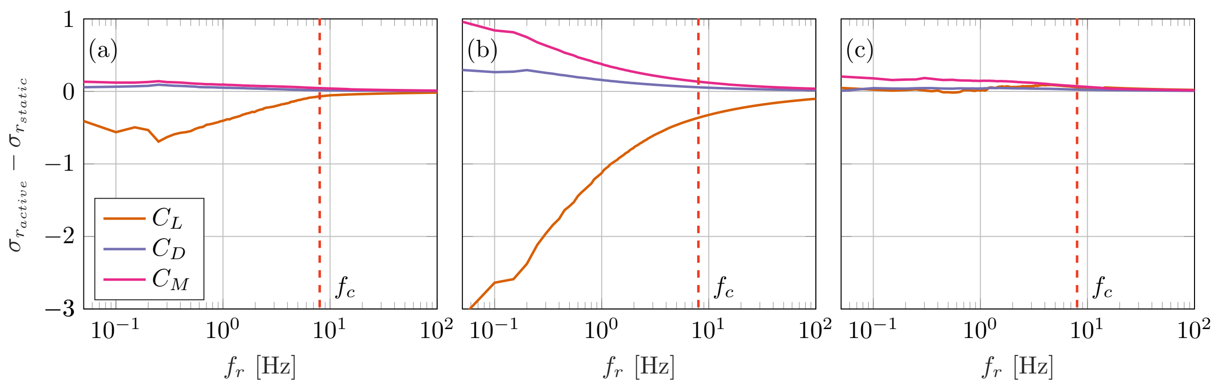
(a)
(b)
(c)
C_L
C_D
C_M
f_c
$\sigma_{r_{active}} - \sigma_{r_{static}}$
f_r [Hz]
1
0
−1
−2
−3
10^{-1}
10^{0}
10^{1}
10^{2}

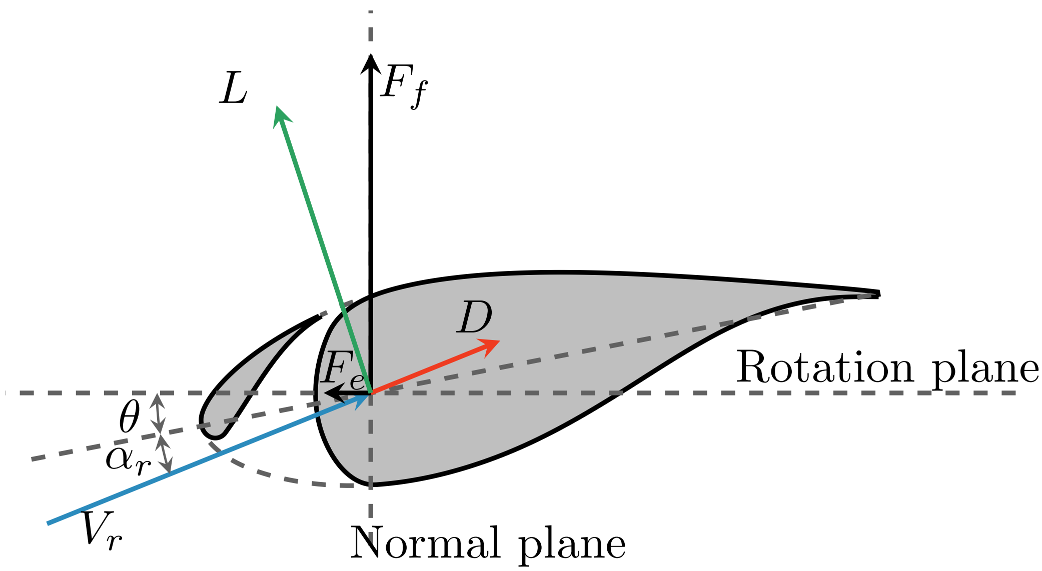
L
F_f
D
F_e
Rotation plane
θ
α_r
V_r
Normal plane

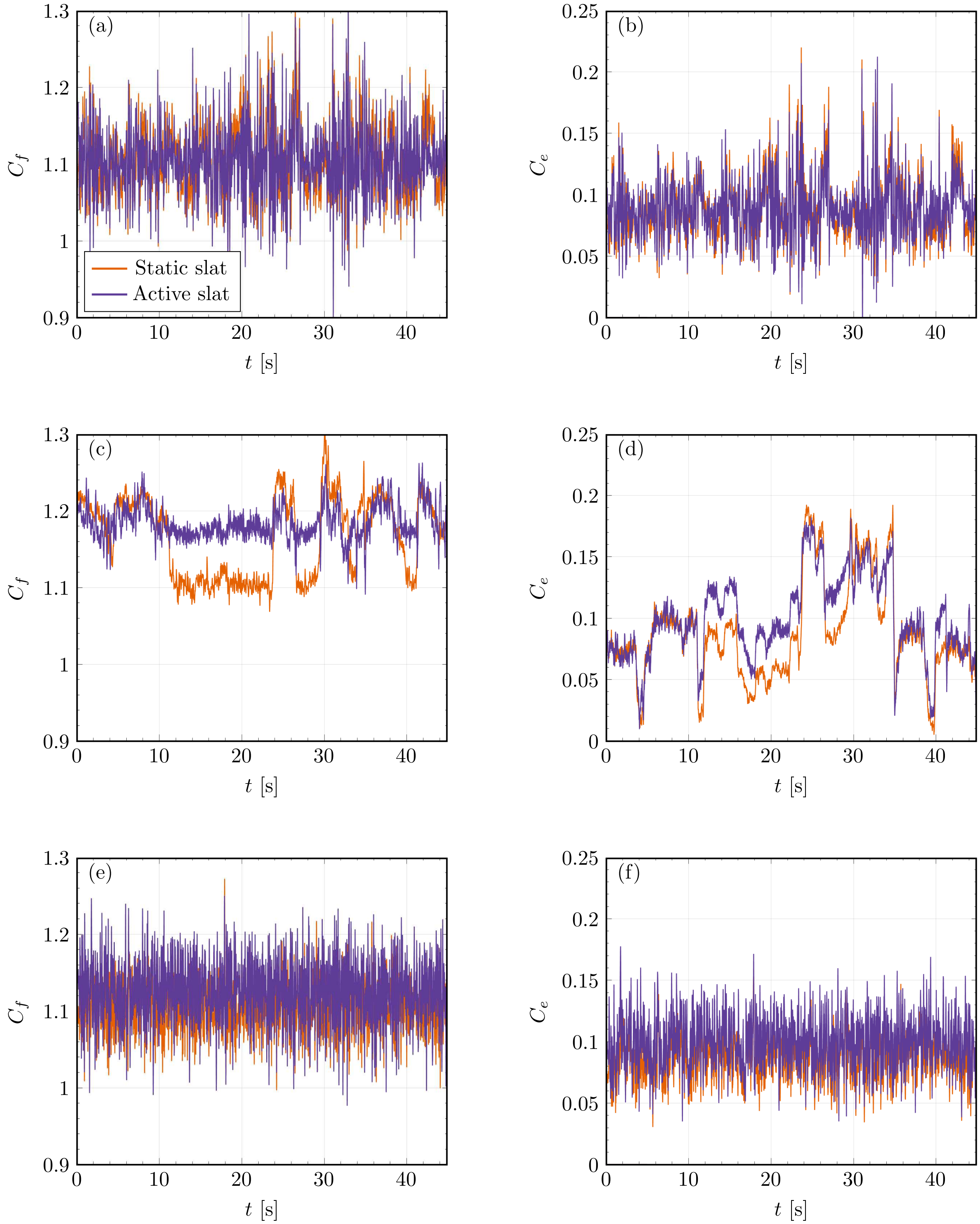
(a)
(b)
(c)
(d)
(e)
(f)
Static slat
Active slat
C_f
C_e
t [s]